A surrogate-assisted uncertainty quantification and sensitivity analysis on a coupled electrochemical–thermal battery aging model

Mohammad Alipour [a,*], Litao Yin [a], Shiva Sander Tavallaey [b,c], Anna Mikaela Andersson [b], Daniel Brandell [a]

[a] *Department of Chemistry - Ångström Laboratory, Uppsala University, 751 21 Uppsala, Sweden*
[b] *ABB AB Corporate Research, Forskargränd 7, SE-721 78 Västerås, Sweden*
[c] *Department of Mechanics, School of Science KTH, SE-100 44 Stockholm, Sweden*

HIGHLIGHTS

- A surrogate-based uncertainty quantification on a battery aging model was performed.
- A surrogate model was used to address the coupled model's high computational cost.
- Sensitivity analysis was performed to identify the most influential parameters.
- A practical method for developing a reliable, high-fidelity battery aging model.

ARTICLE INFO

ABSTRACT

High-fidelity physics-based models are required to comprehend battery behavior at various operating conditions. This paper proposes an uncertainty quantification analysis on a coupled electrochemical–thermal aging model to improve the reliability of a battery model, while also investigating the impact of parametric model uncertainties on battery voltage, temperature, and aging. The coupled model's high computing cost, however, is a significant barrier to perform uncertainty quantification (UQ) and sensitivity analysis (SA). To address this problem, a surrogate model – i.e, by simulating the outcome of a quantity of interest that cannot be easily computed or measured – based on the Gaussian process regression (GPR) theory and principle component analysis (PCA) is built, using a small collection of finite element simulation results as synthetic training data. In total, 43 variable electrochemical–thermal parameters as well as 13 variable aging parameters are studied and estimated. Moreover, the trained surrogate model is also used in the parameterization of the electrochemical and thermal models. The results show that the uncertainties in the input parameters significantly affect the estimations of battery voltage, temperature, and aging. Based on this sensitivity analysis, the most influential parameters affecting the above mentioned battery outputs are reported. This approach is thereby helpful for developing robust and reliable high-fidelity battery aging models with potential applications in digital twins as well as for synthetic data generation.

1. Introduction

Because of their high energy density and safety, lithium-ion batteries (LIBs) are extensively used for energy storage, not least in the electromobility sector. In light of their growing use in automotive applications, much attention has been paid to developing effective battery management systems (BMS) capable of estimating battery lifetime and state-of-health (SOH). Advanced BMSs offer smarter and more effective battery management as well as longer battery lifetimes as a result of recent advancements in modeling tools, diagnostics, and knowledge of how batteries degrade [1].

Computer simulations are becoming increasingly popular in the design of complex BMSs that can take the varying battery working conditions into account. These simulations are developed using models that describe the physics of the real battery system mathematically, as well as on some numerical techniques that enable the transformation of a set of governing partial differential equations into algebraic equations [2]. Due to the complexity of real-world battery systems, taking every detail into account while developing the model would increase the model complexity and thereby the simulation computational cost;

Nomenclature

A	Sandwich area of the cell
a_s	Specific surface area of electrode
b	Bruggeman coefficient
c	Ion concentration
C_p	Heat capacity
D	Diffusion coefficient
E_a	Activation energy
F	Faraday constant
$f_{\mp}$	Average molar activity coefficient
h_{conv}	Convective heat transfer coefficient
i	Current density
I_{app}	Applied current of the cell
i_0	Exchange current density of intercalation
j	Local current density
k_0	Reaction rate constant
k_T	Thermal conductivity
L	Thickness of micro cell
M	Molecular weight
n	Number of Li ions
Q	Capacity of the cell
q_{rev}	Reversible heat generation rate
q_{irr}	Irreversible heat generation rate
q_{ohm}	Ohmic heat generation rate
r	Coordinate along the radius of electrode particle
R	Universal gas constant
R_{film}	Film resistance
R_s	Radius of spherical electrode particle
t	Time
T	Cell temperature
t_0^+	Transference number
T_∞	Ambient temperature
U_{eq}	Equilibrium potential
V	Cell voltage
$\tilde{V}_e$	Molar volume of electrolyte
x	Stoichiometric number in anode
y	Stoichiometric number in cathode

Greek symbols

α	Transfer coefficient for an electrode reaction
δ	Thickness
ε	Volume fraction of a porous medium
η	Overpotential
κ	Ionic conductivity of electrolyte
ρ	Density
σ_s	Solid phase conductivity
Φ	Potential

Subscripts/Superscripts

0	Initial state
i	Index
int	Li ion intercalation
iso	Isolation
l	Liquid phase
lpl	Lithium plating
max	Maximum
min	Minimum
n	Negative electrode
p	Positive electrode
ref	Reference
s	Solid phase
SEI	Solid electrolyte interphase

thus, simplifications and assumptions must be made during the model-building process. However, the model's predictions become uncertain as a result of each simplification and assumption. Furthermore, the model uncertainty is influenced by the fact that many model parameters are empirical constants obtained from limited experimental results, and one single parameter is often used to describe complex and variable properties. Additionally, the initial and boundary conditions of the simulation are inherently uncertain because they are the outcome of experimental measurements. In this context, modelers and scientists have debated the topic of model indeterminacy widely. Generally, most modelers believe that a model cannot be validated in the sense of being proven true; instead, it is more acceptable to say that the model has been extensively corroborated, meaning that it has passed a series of tests [3].

Computational models can be divided into three categories: physics-driven models, data-driven models, and hybrid models that combine the two categories. The physics-driven models integrate acknowledged laws of physics that have been connected with it in an attempt to predict the battery system's behavior. The data-driven method, on the other hand, aims to consider the battery system as a "black box" and statistically infer its features. Data-driven models can quite well capture the behavior of a system; nevertheless, they usually lack physical meaning and require large amounts of test data for training. Physics-based models, on the other hand, are often over-parameterized, but have a great potential to explain the battery system also under previously unobserved situations [4,5]. As a result, major attempts have been made to integrate data-driven models with physics-based models. One notable effort across many scientific and engineering areas is the use of surrogate models to mimic and capture the functional properties of the usually computationally expensive simulation models. For instance, Sinai et al. [6] used neural networks as an approximation in their numerical method for partial differential equations (PDEs). Mckay et al. [7] used a Deep Neural Network-based surrogate model to predict the dynamics of LIBs. They trained the surrogate model using synthetic data generated by the single particle model (SPM). Zhou et al. [8] used a surrogate-assisted teaching–learning optimization technique to effectively parameterize the electrochemical battery model. Zheng et al. [9] used surrogate models to perform uncertainty quantification (UQ) analysis to assess the impact of various design factors on the performance of the structured Si anode system. Here, we build upon these previous efforts by extending the application of surrogate-assisted model approach to a coupled electrochemical–thermal model for battery aging. The surrogate model is trained through a machine-learning type of approach using synthetic data from the battery aging model.

A surrogate-based approach is used in this paper to improve the quality of a high fidelity battery aging model via an uncertainty quantification study followed by parameter optimization of the electrochemical–thermal model. To that end, the design of experiment (DoE) method known as Latin hypercube sampling (LHS) is used to generate input for the parametric sweep study, utilizing a high fidelity battery model based on finite element methods (FEM). To emulate the FEM model outputs for different quantities of interest (QoI) collected by the parametric sweep study, a computationally efficient surrogate model based on GPR theory and PCA is used. The aging parameters were not optimized at this stage due to the dynamic nature of these
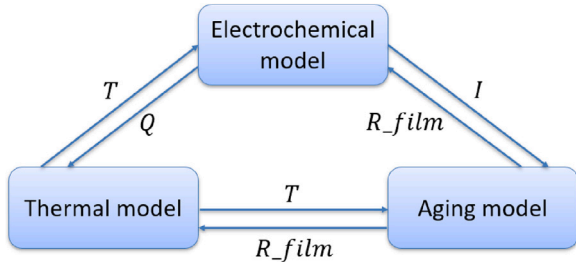
Fig. 1. Schematic of the coupled electrochemical–thermal-aging model.

parameters, that can only be captured and eventually calibrated over long aging cycles. However, after calibration of the electrochemical and thermal parameters, battery aging was implemented into the model. Prior to the optimization of the electrochemical–thermal parameters, a plausibility analysis is proposed using the outcome from surrogate-based sensitivity analysis in order to avoid a complex multi-objective optimization. The rest of this paper is structured as follows: the coupled electrochemical–thermal-aging model is described in Section 2; Section 3 discusses the proposed method's framework and methodology; Section 4 analyzes the findings; and Section 5 concludes this work.

2. Coupled electrochemical–thermal-aging model

LIB behavior is a complex, highly non-linear process that depends on a number of variables, e.g. operating temperature and charge/discharge current rate. Like their electrochemical behavior, their aging rate trajectory is nonlinear and undergoes significant changes over cycling time. The Doyle–Fuller–Newman (DFN) or pseudo-2D (P2D) electrochemical model are the most common physics-based models for studying the behavior of LIBs [10,11]. In this regard, a coupled electrochemical–thermal aging model for a commercial LG 18650 HE4 2.5 Ah Li-ion cell is constructed which includes the DFN (P2D) electrochemical model, a 2D lumped thermal model, and an aging model which is based on side reactions [12,13]. A two-way approach is used for coupling the electrochemical–thermal-aging model, as illustrated in Fig. 1. The governing PDE equations were solved using the finite element method in the COMSOL 6.0 software.

2.1. P2D electrochemical model

The P2D model is governed by a set of partial differential equations (PDEs) that define mass, charge, and energy conservation principles, as well as electrochemical kinetics. Using the P2D model, the battery terminal voltage can be computed as a function of the open circuit potential, the overpotential, the electrolyte potential, and the voltage drop due to film resistance (see Eqs. (32)–(34)) as:

$$V(t) = \Phi_{s,p}(x,t)|_{x=L} - \Phi_{s,n}(x,t)|_{x=0} - R_{film}i_{app}$$
$$= (\eta_p + \Phi_{l,p}(x,t) + U_{eq}^p) - (\eta_n + \Phi_{l,n}(x,t) + U_{eq}^n) - R_{film}i_{app} \quad (1)$$

2.1.1. Electrochemical kinetics at the interface

The local or intercalation current density represents the molar fluxes of charges moving between the active material in each electrode and in the electrolyte. The main intercalation reaction occurs at the particle's surface, and the associated current density j_{int} is governed by a Butler–Volmer type kinetic expression as

$$j_{int} = i_0 \left(\exp\left(\frac{\alpha_a F}{RT}\eta\right) - \exp\left(\frac{\alpha_c F}{RT}\eta\right) \right) \quad (2)$$

where i_0 represents equilibrium exchange current density and is given as:

$$i_{0,i} = k_0 F c_l^{\alpha_a} \left(c_{s,max} - c_{s,surf}\right)^{\alpha_a} c_{s,surf}^{\alpha_c} \quad (3)$$

2.1.2. Charge conservation

There are two types of current densities in LIBs: the electronic current density in the solid phase i_s and the ionic current density in the electrolyte phase i_l. The charge conservation equation governing these two current sources is:

$$\nabla \cdot i_s + \nabla \cdot i_l = 0 \quad (4)$$

$$\nabla \cdot i_s = -a_s j \quad (5)$$

$$\nabla \cdot i_l = a_s j \quad (6)$$

The electron transport in the solid electrode is governed by Ohm's law as

$$i_s = -\sigma_s^{eff} \nabla \Phi_s \quad (7)$$

Li ions are transported in the electrolyte phase via diffusion and electromigration, which are caused by the current flux at the electrode/electrolyte interface. Thus, the ionic current density is governed as

$$i_l = -\sigma_l^{eff} \nabla \Phi_l + \frac{2RT\sigma_l^{eff}}{F} \left(1 + \frac{\partial \ln f_\pm}{\partial \ln c_l} \right)(1-t_+)\nabla(\ln c_l) \quad (8)$$

2.1.3. Mass conservation

The lithium ion concentration in the active materials particles is modeled by Ficks's second law, describing diffusion of Li ions into spherical electrode particles by relating the time derivative to the gradient and diffusion constant as

$$\frac{\partial c_s(x,r,t)}{\partial t} = \frac{1}{r^2}\frac{\partial}{\partial r}\left(D_s r^2 \frac{\partial c_s(x,r,t)}{\partial r}\right) \quad (9)$$

Because of symmetry, the gradient at the particle center is considered to be zero, whereas it is set to the molar flux at the particle surface. As a result, the boundary conditions and initial values become:

$$\frac{\partial c_s(x,r,t)}{\partial r}\Big|_{r=0} = 0, \ D_s\frac{\partial c_s(x,r,t)}{\partial r}\Big|_{r=R} = -\frac{j}{F}, c_s(x,r,0) = c_{s,0} \quad (10)$$

Li concentration in the electrolyte phase depends on ionic current density and is expressed as:

$$\varepsilon_l \frac{\partial c_l(x,t)}{\partial t} = -\nabla \cdot \left(-D_l^{eff}\nabla c_l(x,t) + \frac{i_l t_+}{F} \right) + \frac{a_s j}{F} \quad (11)$$

2.2. Thermal model

LIBs generate a significant amount of heat during cycling, causing the battery temperature to fluctuate. Most electrochemical and aging parameters are temperature dependent, so accurately estimating battery temperature is critical in battery behavior modeling. The energy balance for the battery cell is given as

$$\rho c_p \frac{\partial T}{\partial t} - k\nabla^2 T = q_{rev} + q_{irrev} + q_{ohm} \quad (12)$$

where the reversible entropic heat (q_{rev}), the irreversible reactions heat (q_{irrev}), and the ohmic heat (q_{ohm}) are primary heat generation sources, and are given as

$$q_{rev} = a_s j_{int} T \frac{\partial U_{eq}}{\partial T} \quad (13)$$

$$q_{irrev} = a_s j_{int}\eta \quad (14)$$

$$q_{ohm} = -i_s \cdot \nabla \Phi_s - i_l \cdot \nabla \Phi_l \quad (15)$$

The physical properties of the cell stack are taken as lumped variables, and given as [14]:

$$\rho_{stack} = \frac{\Sigma_i L_i \cdot \rho_i}{L_{stack}} \quad (16)$$
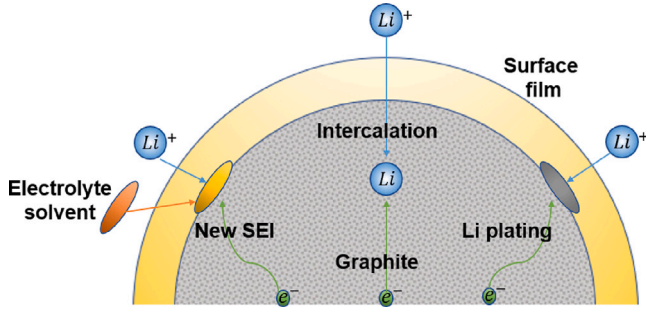
Fig. 2. Schematic of side reactions happening on a graphite particle.

$$C_{p,stack} = \frac{\Sigma_i L_i \cdot \rho_i \cdot C_{p,i}}{L_{stack} \cdot \rho_{stack}} \tag{17}$$

$$k_{T\perp} = \left(\frac{1}{L_{stack}} \cdot \Sigma_i \frac{L_i}{k_{T,i}} \right)^{-1} \tag{18}$$

$$k_{T\parallel} = \frac{\Sigma_i L_i \cdot k_{T,i}}{L_{stack}} \tag{19}$$

where $k_{T\perp}$ denotes the cross-plane thermal conductivity, $k_{T\parallel}$ denotes the in-plane thermal conductivity, and the thickness of the cell stack is given as $L_{stack} = L_{cc^-} + 2(L_{neg} + L_{sep} + L_{pos}) + L_{cc^+}$.

2.3. Aging model

Physical models are critical for understanding the mechanisms of battery aging and predicting battery aging behavior under unanticipated working conditions. This paper considers four major aging mechanisms, which are discussed further in this section. It is often considered that passivisation film formation on the negative electrode is the primary cause of aging in LIBs, resulting in capacity and power losses. The electrolyte solvent components are reduced at the anode particles' surface in a side reaction with Li ions and injected electrons because the anode operating voltage exceeds the electrolyte component's stability window [15]. Despite the fact that multiple reactions have been known to occur depending on the local voltage and surface chemistry, most researchers have modeled this primarily as the reaction between ethylene carbonate (EC) and Li ions [13,16]:

$$2C_2H_4CO_3 + 2e^- + 2Li^+ \rightarrow (CH_2OCO_2Li)_2 + C_2H_4 \tag{20}$$
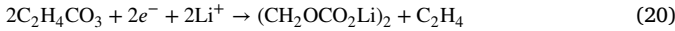
The solid product of the above mentioned side reaction deposits on the anode particle's surface, forming the solid electrolyte interphase (SEI). These deposits build up on the surface of anode particles, causing the SEI layer to develop constantly during battery operation. SEI layers are electronic insulators that, when they are completely coated, can fully isolate certain particles from electronic wiring, resulting in a loss of active carbon material and, thereby, capacity fading. Furthermore, side reactions deplete ions and electrolyte solvents, contributing to additional capacity fade [17]. The other side reactions occurring on the negative electrode surface are lithium plating and stripping. To avoid model complexity, Li stripping was not considered in this work. Li plating occurs when the local anode potential becomes negative vs. Li/Li$^+$, as described by Eq. (21). Fig. 2 illustrates the formation of the SEI layer and Li plating on a graphite particle surface.

$$Li^+ + e^- \rightarrow Li \tag{21}$$

2.3.1. SEI layer growth and Li plating

The total local current density of the negative electrode is determined by three sources: Li intercalation, SEI formation, and Li plating.

$$j_n = j_{int,n} + j_{SEI} + j_{lpl} \tag{22}$$

While side-reactions at the positive electrode are often significant aging factors, we have chosen to neglect them partly for model simplicity, and partly since the side-effects at the anode are generally more dominating. For example, the solvent may be oxidized at the positive electrode, similar to how solvent reduction occurs at the negative electrode, resulting in the formation of the cathode electrolyte interface (CEI). In the research conducted by Lin et al. [18], a simple Tafel equation is proposed as a kinetically limited model for this aging mechanism. Furthermore, this reaction produces H$_2$ which can result in HF, facilitating the dissolution of Mn from the positive electrode [18]. Some other researchers [19] propose that Mn dissolution has a secondary effect, such as promoting SEI growth. Therefore, Li intercalation/deintercalation is presumed to be the only reaction source contributing to the local current density at the cathode.

$$j_p = j_{int,p} \tag{23}$$

As a result of these assumptions, the overpotentials in the negative and positive electrodes are governed as

$$\eta_n = \Phi_{s,n} - \Phi_{l,n} - U_{eq}^n - R_f \frac{j_n}{a_{s,n}} \tag{24}$$

$$\eta_p = \Phi_{s,p} - \Phi_{l,p} - U_{eq}^p \tag{25}$$

The formation of new SEI at the anode surface is determined by both the EC diffusion rate across the surface film [20,21], as well as the interfacial kinetics [22]. Reniers et al. [13] proposed the following equation for j_{SEI} by assuming a constant bulk concentration of solvent $c_{EC,bulk}$ and a linear diffusion rate across the passivation film that incorporates both the kinetically limited SEI layer growth term as well as the limitation term caused by diffusion of electrolyte solvent through the passivation film:

$$j_{SEI} = -\frac{c_{EC,bulk}}{\frac{1}{n_{SEI}Fk_{0,SEI}\exp\left(-\frac{\alpha_{c,SEI}n_{SEI}F}{RT}\eta_{SEI}\right)} + \frac{\delta_{film}}{n_{SEI}FD_{EC}}} \tag{26}$$

where the SEI overpotential is given as:

$$\eta_{SEI} = \Phi_{s,n} - \Phi_{e,n} - U_{eq}^{SEI} - R_{film}\frac{j_n}{a_{s,n}} \tag{27}$$

Similarly, the local current density and overpotential of side reactions due to Li plating are given as

$$j_{Li} = i_{0,Li}\exp\left(-\frac{\alpha_{c,Li}n_{Li}F}{RT}\eta_{Li}\right), \tag{28}$$

$$\eta_{Li} = \Phi_{s,n} - \Phi_{l,n} - R_{film}\frac{j_n}{a_{s,n}} \tag{29}$$

A resistive film is formed on an anode active material at a rate proportional to the side reaction current density as [21]:

$$\frac{\partial c_{SEI}}{\partial t} = -\frac{j_{SEI}}{n_{SEI}F} - \frac{j_{Li}\beta}{n_{SEI}F} \tag{30}$$

$$\frac{\partial c_{Li}}{\partial t} = -\frac{j_{Li}}{n_{Li}F}(1-\beta) \tag{31}$$

where c_{SEI} and c_{Li} denote the molar concentrations of SEI species and lithium metal per unit volume of the electrode, and the β parameter denote the fraction of plated lithium that is oxidized in contact with the electrolyte to form new SEI.

As stated above, the surface film coating on the graphite particles is made up of SEI and Li metal. The fraction of the film that is coating the

particle surface, and hence the film thickness, is proportional to c_{SEI} and c_{Li} as

$$\Delta\varepsilon_{film} = \Delta\varepsilon_{SEI} + \Delta\varepsilon_{Li} = \left(\frac{c_{SEI} M_{SEI}}{\rho_{SEI}} + \frac{c_{Li} M_{Li}}{\rho_{Li}} \right) \tag{32}$$

$$\Delta\delta_{film} = \frac{\Delta\varepsilon_{film}}{a_s} \tag{33}$$

where the film resistance is given as

$$R_{film} = \frac{\delta_{film}}{\kappa_{SEI}} = \frac{\delta_{0,SEI} + \Delta\delta_{film}(t)}{\kappa_{SEI}} \tag{34}$$

In Eq. (34), $\delta_{0,SEI}$ refers to the thickness of the SEI layer formed initially during the formation period and $\Delta\delta_{film}$ refers to change in the thickness of the film caused by the products formed during charging.

2.3.2. Electrolyte loss

The electrolyte depletion due to side reactions is modeled as [23, 24]:

$$\Delta\varepsilon_l = -\frac{\alpha \tilde{V}_l (Q_{SEI} + \beta Q_{Li})}{A\delta_- F} \tag{35}$$

where α is a coefficient denoting the number of moles of electrolyte consumed per mole of lithium ion consumed and $\tilde{V}_e$ is the molar volume of electrolyte. Q_{SEI} and Q_{Li} denote ionic losses due to SEI layer growth and Li plating, respectively, and are given as

$$Q_{SEI}(\tau) = -\int_{x=0}^{\delta_-} \left(\int_{t=0}^{\tau} j_{SEI}(x,\tau) d\tau \right) A dx \tag{36}$$

$$Q_{Li}(\tau) = -\int_{x=0}^{\delta_-} \left(\int_{t=0}^{\tau} j_{lp}(x,\tau) d\tau \right) A dx \tag{37}$$

2.3.3. Insulation of the active material

The passivation film can prevent some graphite particles from participating in Li^+ intercalation and deintercalation. The loss of active material as a result of insulation by newly generated products from side reactions is calculated as follows [24,25]:

$$\Delta\varepsilon_s = \Delta\varepsilon_{film} \alpha_{iso} \tag{38}$$

2.3.4. Capacity loss

The side reactions discussed in this section have an impact on battery performance. While loss of Li ions due to SEI layer growth and Li plating, as well as insulation of active material, result in capacity loss, passivation layer growth and electrolyte losses result in increased resistance and consequently power fade [23]. The capacity of a fresh cell could be stated as

$$\begin{aligned} Q_{fresh} &= (y_{max} - y_{min})\varepsilon_{s,0,p}\delta_p A_p c_{s,max,p} F \\ &= (x_{max} - x_{min})\varepsilon_{s,0,n}\delta_n A_n c_{s,max,n} F \end{aligned} \tag{39}$$

where y_{max} and y_{min} correspond to maximum and minimum stoichiometric coefficients in the cathode, and x_{max} and x_{min} correspond to maximum and minimum stoichiometric coefficients in the anode, respectively. With the cell being cycled, Li ions are lost due to side reactions on the anode side resulting in capacity fade. Therefore, the capacity of the aged cell could be estimated as:

$$Q_{aged} = (x + x_{shift} - x_{min})(\varepsilon_{s,0,n} + \Delta\varepsilon_{s,n})\delta_n A_n c_{s,max,n} F \tag{40}$$

where

$$x_{shift} = \frac{Q_{SEI} + Q_{Li}}{(\varepsilon_{s,0,n} + \Delta\varepsilon_{s,n})\delta_n A_n c_{s,max,n} F} \tag{41}$$

2.4. Parameter classes

Battery models, which provide information on a system's predicted range, safe operation limits, and optimal usage conditions, can describe a system in different degrees of detail. Traditional BMS operational models commonly include equivalent circuit models (ECMs) or empirical models. Because these model parameters often lack electrochemical significance or rather only roughly capture the electrochemical phenomena, these models can merely predict the behavior of LIB cells under specific operating conditions for which test data is available. Another factor that these models generally fail to consider is degradation. High-fidelity electrochemical aging models instead have the ability to accurately predict battery behavior under a wide range of unforeseen operating conditions. However, the main obstacle to applying high fidelity models in BMSs, beside the demanding computation capacity, is model parameterization. On the other hand, the influence of different parameters in high-fidelity models are not equal, which means that some have a greater impact on the model's output. To understand this, it is critical to investigate the impact of parametric model uncertainties on the electrochemical, thermal, and aging behavior of the battery under various operating conditions. For such a study, it is vital to know the lower and upper boundaries that could be considered for the model's various parameters. A literature review has therefore been conducted in this regard in order to obtain a valid parameter window used for studied NMC cells. Some parameters, such as electrode geometric parameters and open circuit voltage (OCV) curves, were experimentally measured after cell disassembly. Electrode coating thickness and active material particle sizes were measured using scanning electron microscopy (SEM). In this measurement, samples from various parts of the electrodes were collected (see the supplementary information for details). The result of that study is listed in Table 1.

Some of the parameters listed in Table 1 are functions of temperature and electrolyte phase concentration, which could be expressed using the Arrhenius law expressions listed in Table 2.

3. Methodology

The output of the coupled electrochemical–thermal-aging model may deviate from measurements taken from real-world battery systems due to, for example, uncertainties in model input parameters and design specifications. A good understanding of the influence of these uncertainties is required for the reliable design of high-fidelity models used for an in-depth understanding of the aging behavior of battery systems. Uncertainty quantification is a powerful tool to study the propagation and impact of different model parameters' fluctuation and inaccuracy on the model output. In this context, the key challenge is to get access to a reliable and computationally affordable emulator (i.e., a surrogate) that can be used for the desired study. Fig. 3 shows the flowchart for uncertainty quantification analysis performed in this work (ECT stands for Electrochemical–thermal model). The SmartUQ software was used in different steps of the analysis as described below.

3.1. Input space and design of experiment

The parameters and corresponding intervals of variation listed in Table 2 were used to define the input space. The design of experiment (DOE) and data sampling are the first steps in building surrogate models. To that end, the training dataset is defined as follows: Let X represent the N-dimensional hypercube (i.e., the FEM model's input space), and let $\mathbf{x} = (x_1, \ldots, x_n)$ represent a point in X where n denotes the number of uncertain input parameters. The Latin hypercube sampling (LHS) [43] method was employed to draw N samples from X, and subsequently, the training input data are arranged in the matrix $\mathbf{X}$, so-called experimental design, as:

$$\mathbf{X} = (\mathbf{x}^{(1)}, \ldots, \mathbf{x}^{(N)}) \subset R^{N \times n} \tag{42}$$

Table 1

A range of electrochemical and aging parameters used in literature for the NMC/graphite cells.

Parameters	N_cc	Neg	Sep	Pos	P_cc	References
Known parameters/constants						
V_{max} [V]	4.2					
V_{min} [V]	2.5					
F [C mol^{-1}]	96 487					
R [J mol^{-1} K^{-1}]	8.314					
T_0 [K]	303.15					
T_{ref} [K]	298					
Geometric parameters						
A [m^2]	0.05723	0.05428	0.06195	0.05192	0.05192	Measurement
L [μm]	11	[48–53]	12	[62–68]	10	SEM
Measurement						
R_s [μm]		[4.8–30]		[4.5–19]		SEM
$\varepsilon_{s,0}$		[0.4–0.694]		[0.35–0.745]		[14,17,23–31]
$\varepsilon_{l,0}$		[0.21–0.5]	[0.4–0.55]	[0.17–0.45]		[14,17,21,23–31]
Transport parameters						
b		[1.3–1.86]	[1.3–1.7]	[1.3–2.26]		[14,17,23,27,28,32]
$D_{s,ref}$ [m^2 s^{-1}]		[1e–14–3e–13]		[1e–14–5e–13]		[14,24,26,27,30,31,33,34]
$E_a^{D_s}$ [J/mol]		[10 000–45 000]		[10 000–45 000]		[14,17,26,28,31,32,34,35]
$D_{l,ref}$ [m^2 s^{-1}]		[1e–11–4.5e–10]	[1e–11–4.5e–10]	[1e–11–4.5e–10]		[17,23,24,26,27,32]
$E_a^{D_l}$ [J/mol]		[12 360–15 000]	[12 360–15 000]	[12 360–15 000]		[26,35]
$f_{\mp,ref}$		1	1	1		COMSOL database
$E_a^{f_\mp}$ [J/mol]		1000	1000	1000		COMSOL database
σ_s [S m^{-1}]	[5.8e7–6e7]	100		[0.17–10]	[3.4e7–3.7e7]	[14,17,23,25,27,29–33,36]
$\sigma_{l,ref}$ [S m^{-1}]		0.17	0.17	0.17		[26]
$E_a^{\sigma_l}$ [J/mol]		4.2e4	4.2e4	4.2e4		[26]
t_0^+		[0.25–0.45]	[0.25–0.45]	[0.25–0.45]		[17,23,24,26–33]
Kinetic parameters						
α_a		0.5		0.5		[23–25,28,30–32]
α_c		0.5		0.5		[23–25,28,30–32]
$k_{0,ref}$ [mol$^{-0.5}$ m$^{2.5}$ s^{-1}]		[4e–12–2e–10]		[0.7e–11–1.1e–10]		[14,24,26,27,29–31,34]
$E_a^{k_0}$ [J/mol]		[30 000–45 000]		[23 000–39 570]		[14,26,28,31,32,34]
Concentration parameters						
$c_{s,max}$ [mol m^{-3}]		[32 000–35 000]		[48 000–52 500]		[14,24,27–33]
SOC_0		[0.76–0.936]		[0.39–0.52]		[21,29–31,33,35]
$c_{l,0}$ [mol m^{-3}]		[1000–1200]	[1000–1200]	[1000–1200]		[23–28,31,32]
$Stoichiometry 100\% SOC$		[0.672–0.88]		[0.222–0.442]		[14,17,23,25]
$Stoichiometry 0\% SOC$		[0.002–0.2]		[0.936–0.996]		[14,17,23,25]
Physical						
C_p [J/(kg K)]	385	[867–1013]	[1704–1978]	[840–912]	900	[14,28]
h_{conv} [W/(m K)]						
k_T [W/(m^2 K)]	398	[0.37–1.04]	[0.14–0.33]	[0.43–1.58]	237	[14,28]
ρ [kg m^{-3}]	8900	[1768–2240]	[1009–1081]	[3057–4870]	2700	[14,28,37]
Aging parameters						
α		[0.5–1]				[23,35]
α_{iso}		[0.275–0.75]				[23–25]
$\alpha_{c,SEI}$		[0.5–0.75]				[21,23,24,35]
$\delta_{SEI,0}$ [nm]		[2–10]				[30,33,34]
$k_{0,SEI,ref}$ [m s^{-1}]		[1e–12–1.36e–12]				[21,34,38,39]
$E_a^{k_{0,SEI}}$ [J mol^{-1}]		[30 000–65 000]				[34,35,38]
κ_{SEI} [S m^{-1}]		[3.8e–7–5e–4]				[21,21,23–25,30,32,33,33–35]
n_{sei}	2					
M_{SEI} [kg mol]		0.162				[21,24,25,30,32–35]
ρ_{SEI} [kg m^{-3}]		1690				[21,24,25,30,32–35]

Table 1 (*continued*).

Parameters	N_cc	Neg	Sep	Pos	P_cc	References
U_{eq}^{SEI}		[0.21–0.4]				[17,23,23–25,30,33,33–35,38]
$\tilde{V}_e$ [m³ mol]		[5.6e−5–3.25e−4]				[23–25,35]
$\alpha_{c,Li}$		0.5				[21,31,31]
$i_{0,Li,ref}$ [A m⁻²]		[1e−3–1e−5]				[21,38]
$E_a^{i_{0,Li}}$		[50 000–68 000]				[38]
n_{Li}	1					
M_{Li} [kg mol]		6.94e−3				[21,24,25,30,32–35]
ρ_{Li} [kg m⁻³]		534				[21,24,25,30,32–35]
$c_{EC,bulk}$ [mol m⁻³]		4541				[21,34,39]
$D_{EC,ref}$ [m² s⁻¹]		[6.8e−21–4.9e−19]				[21,34,38,39]
$E_a^{D_{EC}}$		[20 000–30 000]				[38]
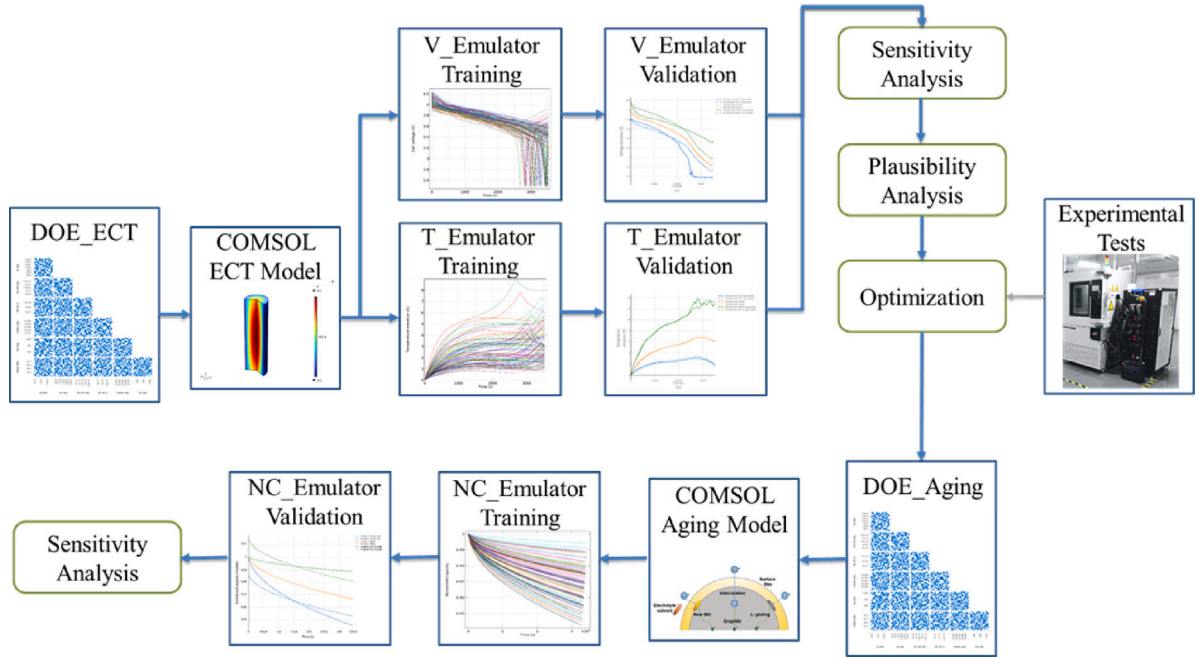
Fig. 3. Uncertainty quantification flowchart. ECT stands for Electrochemical–thermal model.

Table 2

Temperature and concentration dependency of parameters.

Parameter	Temperature-dependency function	Reference
$D_{s,pos}$ [m²/s]	$D_{s,ref,p}\exp\left(-\frac{E_a^{D_{s,p}}}{R}(\frac{1}{T}-\frac{1}{T_{ref}})\right)$	[40,41]
$D_{s,neg}$ [m²/s]	$D_{s,ref,n}(\frac{c_l}{1\,[\text{mol m}^{-3}]})\exp\left(-\frac{E_a^{D_{s,n}}}{R}(\frac{1}{T}-\frac{1}{T_{ref}})\right)$	[40]
D_l [m²/s]	$D_{l,ref}(\frac{c_l}{1\,[\text{mol m}^{-3}]})\exp\left(-\frac{E_a^{D_l}}{R}(\frac{1}{T}-\frac{1}{T_{ref}})\right)$	[42]
$k_{0,p}$ [mol⁻⁰·⁵ m²·⁵ s⁻¹]	$k_{0,ref,p}\exp\left(-\frac{E_a^{k_{0,p}}}{R}(\frac{1}{T}-\frac{1}{T_{ref}})\right)$	[40,41]
$k_{0,n}$ [mol⁻⁰·⁵ m²·⁵ s⁻¹]	$k_{0,ref,n}\exp\left(-\frac{E_a^{k_{0,n}}}{R}(\frac{1}{T}-\frac{1}{T_{ref}})\right)$	[40,41]
σ_l [S/m]	$\sigma_{l,ref}(\frac{c_l}{1\,[\text{mol m}^{-3}]})\exp\left(-\frac{E_a^{\sigma_l}}{R}(\frac{1}{T}-\frac{1}{T_{ref}})\right)$	COMSOL database
$f_{\mp}$	$f_{\mp,ref}(\frac{c_l}{1\,[\text{mol m}^{-3}]})\exp\left(-\frac{E_a^{f_\mp}}{R}(\frac{1}{T}-\frac{1}{T_{ref}})\right)$	COMSOL database
D_{EC} [m²/s]	$D_{EC,ref}\exp\left(-\frac{E_a^{D_{EC}}}{R}(\frac{1}{T}-\frac{1}{T_{ref}})\right)$	[42]
$k_{0,SEI}$ [m/s]	$k_{0,SEI,ref}\exp\left(-\frac{E_a^{k_{0,SEI}}}{R}(\frac{1}{T}-\frac{1}{T_{ref}})\right)$	[42]
$i_{0,Li}$ [A/m²]	$i_{0,Li,ref}\exp\left(-\frac{E_a^{i_{0,Li}}}{R}(\frac{1}{T}-\frac{1}{T_{ref}})\right)$	[42]

3.2. FEM model output and training data-sets

For a given experimental design matrix **X**, the FEM solves the coupled electrochemical–thermal-aging model. The FEM model can be regarded as "black box" function M that performs the following mapping from a vector of input parameters **x** to a vector of quantity of interest (QoI) **y**:

$$M : \mathbf{x} \in \mathbf{X} \subset \mathbb{R}^{N \times n} \mapsto \mathbf{y} = \mathrm{M}(\mathbf{x}) \in \mathbf{Y} \subset \mathbb{R}^{N \times t_{last}} \qquad (43)$$

where t_{last} denotes the last time step for a corresponding QoI. The QoIs considered in the FEM model are time-dependent outputs including battery voltage, temperature elevation, and cyclic aging trajectory performed at ambient temperature of 25 °C and discharge rates of 0.5C, 1C, and 2C. The FEM model data are basically input/output values that are collected in an evaluation group as follows:

$$D = \left\{ \left(\mathbf{x}^{(i)}, \mathrm{M}(\mathbf{x}^{(i)})\right), i = 1, \ldots, N \right\} \qquad (44)$$

3.3. Surrogate models

A functional response emulator (FRE) is used to generate the corresponding surrogate models since the QoIs are time-dependent. In contrast to other emulators, FREs consider a functional input variable,

like time. In addition, there is only one response for each output function and functional input variable. The FRE requires three elements to generate the surrogate model: an input matrix, a response matrix, and a time vector. For a given input matrix $\mathbf{X} \subset \mathbb{R}^{N \times n}$, each row represents a different set of inputs, while the input parameters of FREs can each be time dependent vectors. Similarly, for a given output matrix $\mathbf{Y} \subset \mathbb{R}^{N \times t_{last}}$, each row represents the output response from the same row of the $\mathbf{X}$ matrix, and each column represents a value of the QoI, assigned to a time point in the time vector in the same order as the time vector. The surrogate model $\tilde{M}$ is a function that emulates the behavior of the original physical simulator M at a very low computational cost per run which is given as :

$$\tilde{M} : \mathbf{x} \in \mathbf{X} \mapsto \tilde{M}(\mathbf{x}) \tag{45}$$

as a result of which:

$$\tilde{M}(\mathbf{x}) \approx M(x) \tag{46}$$

Surrogate models may be derived utilizing different approaches, such as polynomial chaos expansions, law-rank tensor approximations, Kriging, support vector machines, artificial neural networks, and so on [44]. Kriging (also known as Gaussian process modeling, see details in [45]) is used in this work because it is typically the first option in this context due to its ease of understanding and potency in estimating nonlinear behavior. After collecting data from the FEM model runs on the experimental design, the next step would be to calibrate the surrogate model. Maximum likelihood estimation is used to fit a Gaussian process model to the input matrix generated by the data when estimating the hyperparameters determining the correlation of the underlying Gaussian process.

3.4. Sensitivity analysis

Sensitivity analysis (SA) is used to determine the significance of each input parameter in relation to an output variable. The variance-based global SA is used in this work to define input and output uncertainties as probability distributions. The output variation was then decomposed into its component parts. Each component represents the influence of the input parameter (main effect index) or factors combined (total effect index) on the output variable (see [46]). Using sampling-based sensitivity analysis utilizing corresponding surrogate models, the main and total Sobol indexes are estimated as

$$S_i = \frac{\text{Var}_{\mathbf{x}_i}(\mathbb{E}_{\mathbf{x}_{\sim i}}(\mathbf{y}|x_i))}{\text{Var}(\mathbf{y})} \tag{47}$$

$$ST_i = \frac{\mathbb{E}_{\mathbf{x}_{\sim i}}(\text{Var}_{\mathbf{x}_i}(\mathbf{y}|\mathbf{x}_{\sim i}))}{\mathbf{y}} \tag{48}$$

where S_i, ST_i, $\mathbf{x}_{\sim i}$, $\mathbb{E}$, Var, and $\mathbf{y}$ denote the main effect Sobol index, the total effect Sobol index, the $(n-1)$-dimensional parameter space with all factors but x_i, the expectation operator, the variance, and the output space, respectively. Since SA is probabilistic and can provide a wide range of results, the sensitivity analysis results were displayed as the sample mean of the replications.

4. Results and discussion

Battery models can be applied in a wide range of situations, including electrochemical and thermal behavior prediction, battery state-of-health estimation, charging and discharging procedure optimization, and safety limits calculation. Accuracy of the output, however, might be impacted by battery model uncertainties. The high-fidelity coupled electrochemical–thermal aging model, on the other hand, cannot be directly applied for uncertainty and sensitivity analysis due to the high computational cost. As a result, a surrogate-based model is used to simulate the different quantities of interest from the coupled model. More specifically, this paper examines the effects of Li-ion battery

model uncertainty on battery electrochemical, thermal, and aging estimation. To this end, 43 electrochemicial–thermal parameters as well as 13 aging parameters, with the lower and upper limits as listed in Table 1, are included in the design of experiment. Some geometric parameters, such as particle radius and electrode thickness, are measured experimentally after cell disassembly, while others are imported from a list of NMC cell parameters reported in the literature. Following the derivation of the experimental design using the LHD method, a parametric sweep study in COMSOL was performed at 1C discharge rate to determine the variation in the QoIs, which included cell voltage, temperature elevation, and normalized capacity (aging trajectory). The surrogate models' accuracy was tested using various sample sizes, and no discernible differences were discovered. As a result of limited computational power, sample sizes greater than 200 were not tested. Fig. 4 depicts the effect of parametric model uncertainties on battery voltage (Fig. 4(a)), temperature (Fig. 4(c)), and aging (Fig. 4(e)). As shown by the displayed variations in these figures, uncertainties in input parameters have a significant impact on voltage time outputs in terms of range (x-axis) and battery power output (y-axis), temperature elevations in the 1–9 K range, and normalized capacity (cyclic aging) in the range from 1 down to 0.94 during the first 50 cycles. Following the parametric sweep output from the FEM model, surrogate-based emulators for three different QoIs are trained as voltage-emulator, temperature-emulator, and normalized capacity emulator. Figs. 4(b), 4(d), and 4(f), which are calculated using the 5%, mean, and 95% quantiles of the observed data, show the validation results for the voltage-emulator, temperature-emulator, and cyclic aging-emulator, respectively. The root mean square error (RMSE) for validated emulators are calculated as 0.094, 0.128, and 0.031 for mean voltage emulator, mean temperature emulator, and mean normalized capacity emulator, respectively. In short, the small RMSE values highlight a good validation of the emulated surrogate models for all three QoI.

Sensitivity analysis was carried out following the training of the surrogate models for different QoIs to determine which input parameters have a greater impact on the uncertainty of the model output. Fig. 5 shows the Sobol indeces for the influential parameters with regards to the attributed QoI. Parameters with Sobol index less that 0.005 were dropped and classified as non-influential parameters. It is worth noting that the reported values in the literature for NMC cells with the defined variation range for each specific parameter were used to determine the sensitivity of the parameters. This implies that changing the defined range for each parameter will result in different SA values. According to the SA analysis, the most influential parameters influencing cell temperature are $(k_{0,ref,p})$, (h_{conv}), $(k_{0,ref,n})$, $(R_{s,p})$, $(R_{s,n})$, (L_n), and $(D_{s,ref,p})$ with Sobol indexes greater than 0.1. This is in line with what physical intuition would predict, because reaction rates in the electrodes, convective heat transfer, geometric parameters, and the Li$^+$ diffusion rate in the solid phase are all highly important contributors to heat generation and dissipation in LIBs, and have been extensively analyzed in various high-fidelity models. The active material volume fractions in the positive ($\varepsilon_{s,0,p}$) and negative electrode ($\varepsilon_{s,0,n}$), solid phase conductivity of positive electrode ($\sigma_{s,p}$), initial state of charge of positive electrode $SOC_{0,p}$, and reaction rates in the positive and negative electrodes obviously influence the cell voltage output significantly. Regarding battery aging, the EC diffusion rate across the surface film ($D_{EC,0,p}$), the isolation rate of the passivisation film (α_{iso}), and the equilibrium potential of the SEI reaction (U_{eq}^{SEI}) are the most influential parameters for the normalized capacity variation, implying that SEI layer growth and isolation of the active material are the dominant aging mechanisms.

Using the Multiview feature in Smart UQ, as shown in Fig. 6, the design space of the three most important parameters for each QoI was visualized by showing linked cross-sections. The cross sections show how an output variable responds to changes in an input variable when all other input variables are held constant. Thereby, it can be seen how these different parameters are influential for the respective QoI.
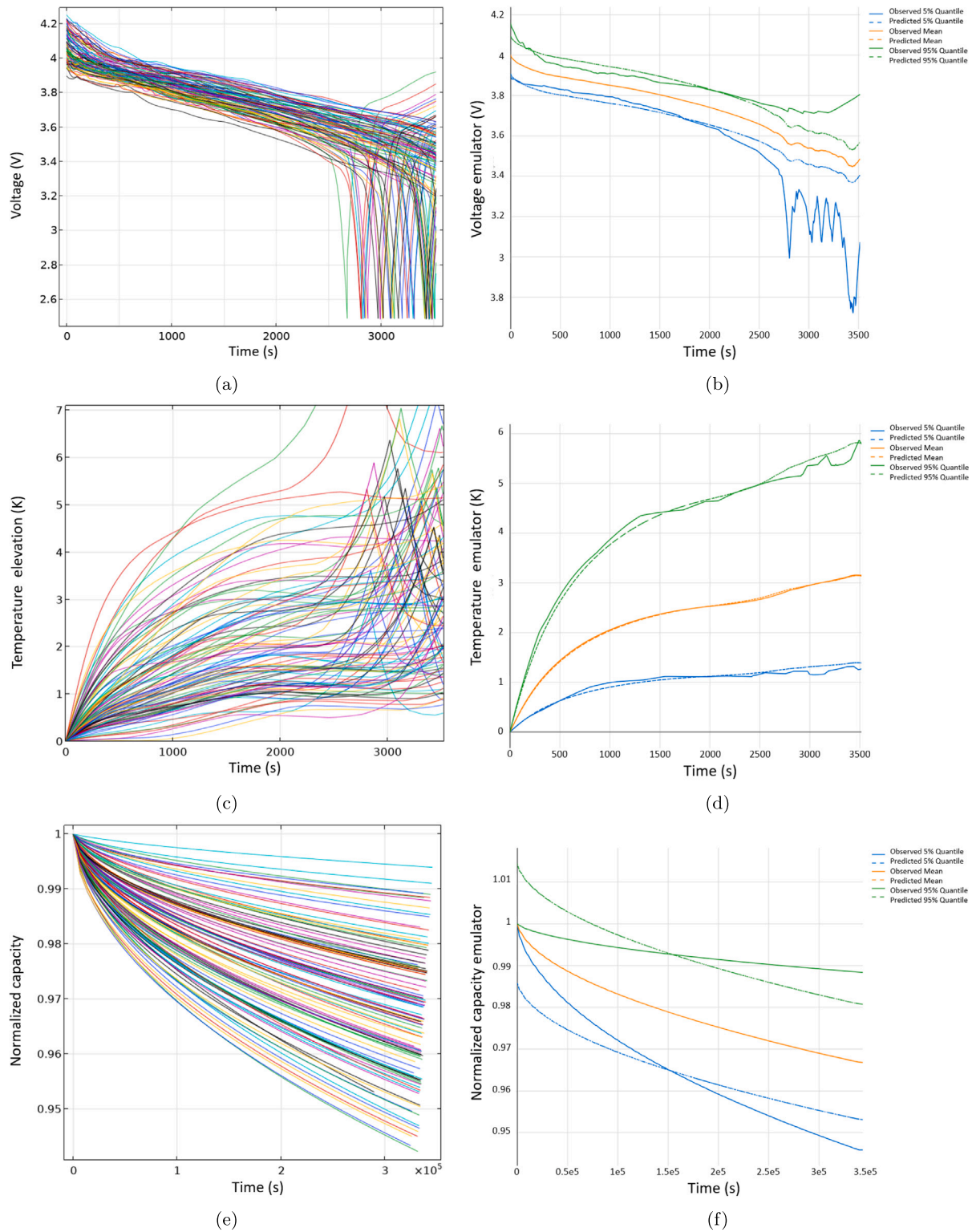
Fig. 4. Parametric sweep outputs for the (a) cell voltage, (c) cell temperature elevation, and (e) normalized capacity, and the corresponding emulators (b, d, f).

Furthermore, functional response data matching was performed to optimize the electrochemical and thermal parameters based on the algorithm shown in Fig. 7. Briefly, a Sobol index (SI) with a threshold of 0.005 is used to classify the parameters into three groups. Non-influential parameters are defined as those with SI less than the threshold for both QoIs. The second class of parameters was influential with respect to one QoI but not with respect to the other, for which the respective emulator was used for calibration. The final class of

parameters were influential on both QoIs for which the emulator with a higher SI is used for calibration. The objective was set to minimize the difference between experimental and simulation results based on the surrogate model as:

$$\Sigma(y_{epxt} - y_{sim})^2 \tag{49}$$

The BOBYQA (bound optimization by quadratic approximation) was used as an optimization method. Table 3 lists the parameters which
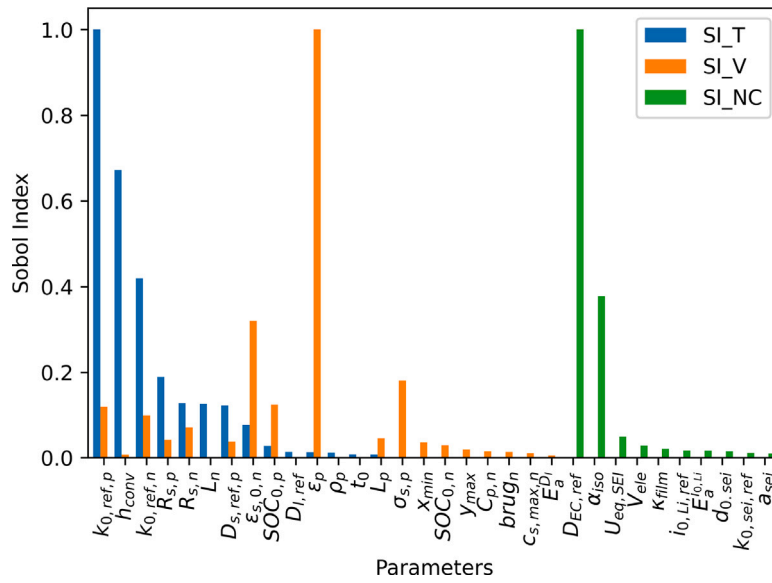
Fig. 5. Sobol Indexes for the influential parameters with regard to temperature, voltage, and normalized capacity outputs.
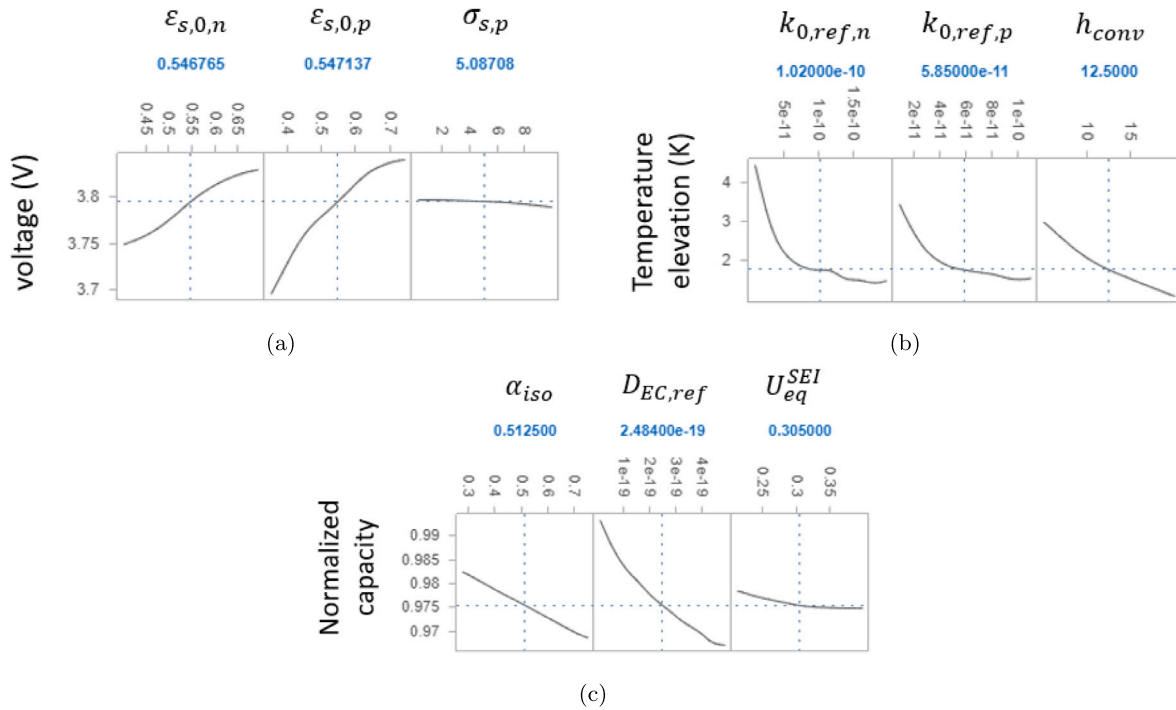

Fig. 6. The cross sections of output variables (QoIs) respond to changes in the three most influential input variables.

were optimized using the voltage and temperature surrogate models (emulators). These parameters are thereby a key output of this surrogate-based optimization, and those best being able to reproduce this specific cell chemistry. As can be seen, the advantage of using this approach is that a large set of parameters can be optimized in a computationally effective way based on a limited number of simulations.

Finally, to validate the surrogate assisted optimization, the voltage and temperature outputs from the coupled FEM model at various discharge rates were benchmarked towards the experimental measurements on the same cell chemistry, as shown in Fig. 8. The experimental voltage and temperature measurements were recorded at the same operating conditions of 25 °C and 0.5C, 1C, and 2C discharge rates.

The results demonstrate a good fit between the measured and simulated data. The quality of the chosen methodology was assessed by calculating the mean absolute errors (MAE). For the voltage responses at 0.5C, 1C, and 2C discharge rates, the MAE values were found to be 0.037, 0.024, and 0.048, respectively. Similarly, for the temperature responses at 0.5C, 1C, and 2C discharge rates, the MAE values were 0.18, 0.12, and 0.27, respectively. The relatively higher MAE values for the temperature can be attributed to the lack of measured potential temperature coefficients (dU/dT) at the electrode levels, resulting in the utilization of the reported values from COMSOL Multiphysics 6.0. Therefore, further improvement is required to enhance the temperature predictions by incorporating more precise information on the temperature coefficients.
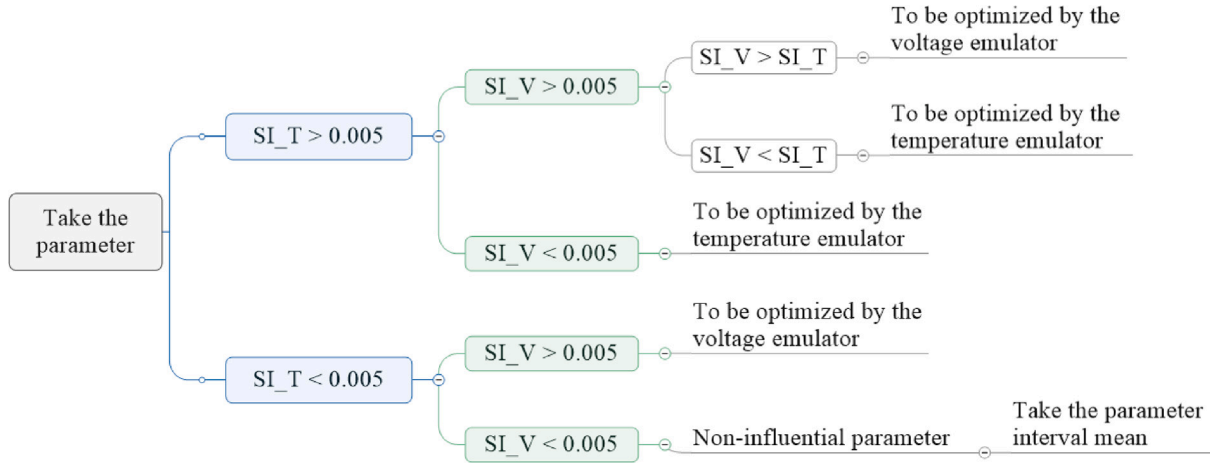
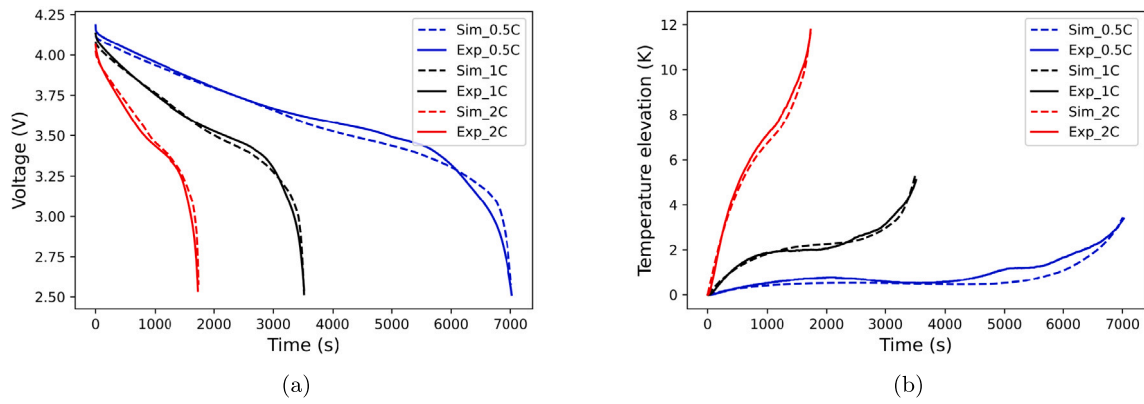Fig. 7. An algorithm for optimizing the electrochemical–thermal model parameters.

Fig. 8. Validation of the experimental (Exp) and simulated (Sim) (a) cell voltage and (b) cell temperature elevation optimized based on the surrogate models.

Table 3
Optimized electrochemical and thermal parameters using the surrogate models.

Optimized by V-Emulator		Optimized by T-Emulator	
Parameter	Value	Parameter	Value
L_p [m]	6.32e−5	L_n [m]	5.05e−5
$\varepsilon_{s,0,n}$	0.528	$R_{s,n}$ [m]	1.21e−5
$\varepsilon_{s,0,p}$	0.352	$R_{s,p}$ [m]	1.182e−5
σ_p [S/m]	9.5	$D_{s,ref,p}$ [m^2 s^{-1}]	1.286e−13
$c_{s,max,n}$ [mol/m^3]	32 560	$D_{l,ref}$ [m^2 s^{-1}]	2.232e−10
$SOC_{0,n}$	0.9004	$k_{0,ref,p}$ [mol$^{-0.5}$ m$^{2.5}$ s^{-1}]	9.69e−11
$SOC_{0,p}$	0.092	$k_{0,ref,p}$ [mol$^{-0.5}$ m$^{2.5}$ s^{-1}]	6.16e−11
x_{min}	0.067	h_{conv} [W m^{-1} K^{-1}]	12.55
y_{max}	0.951	ρ_p [kg m^{-3}]	3963
$C_{p,n}$ [J kg^{-1} K^{-1}]	958.4	t^+	0.35
$brug_n$	1.53		
$E_a^{D_l}$ [J mol^{-1}]	1460		

To evaluate the robustness of the model against parameter variations, we conducted a comprehensive analysis by introducing controlled 10% variations in two key parameters: $k_{0,ref,p}$ and $\varepsilon_{s,0,p}$, known for their influential effects on the model output. The impact of these variations on the temperature and voltage response MAE was then examined. The results clearly demonstrate the model's ability to maintain its performance even in the presence of parameter variations. When introducing a +10% variation in $k_{0,ref,p}$, the observed changes in the temperature MAE were relatively small, with a minor increase of 0.0165 units. The voltage MAE showed an even more negligible

change of 0.0005 units. Similarly, for a +10% variation in $\varepsilon_{s,0,p}$, the model exhibited a slight increase of 0.009 units in the temperature response MAE, while the voltage response MAE changed by 0.006 units. These findings indicate that the model's predictions remain robust and accurate, with minimal deviations even when the influential parameters experience notable variations. The small changes in MAE imply that the model is capable of adapting to parameter variations without significantly compromising its overall performance. However, it is important to note that further investigations and analyses are necessary to thoroughly assess the model's robustness across a wider range of parameter variations and ensure its applicability in diverse scenarios and applications.

5. Conclusions

A surrogate-assisted uncertainty analysis on a physics-based battery aging model was performed with the goal of developing a robust and reliable battery aging model, as well as investigating the impact of parametric model uncertainties on main battery outputs such as voltage, temperature, and aging. Due to the high computational cost of the coupled model, the UQ and SA studies were conducted using a surrogate-assisted approach based on GPA and PCA theory. The electrochemical and thermal models were also calibrated using the surrogate model and experimental measurements. As the aging parameters evolve during cycling, the calibration of the aging parameters can be performed as a continuation of this work in the future in the form of online learning. The result showed that minor uncertainties in the physical battery model's input parameters cause large variations in battery performance and aging trajectory. However, the impact

of individual input parameters may differ depending on the type of quantity of interest. Therefore, sensitivity analysis was performed to identify the most influential input parameters affecting various QoIs by computing the Sobol indexes. Based on the results, the active material volume fractions, reaction rates, diffusion coefficient of EC in SEI film, heat transfer coefficient, solid phase conductivity, isolation coefficient of passivisation film, and equilibrium potential of SEI formation are the most influential parameters affecting battery performance and aging. This methodology, as a complement to previous studies in the field, paves the way for the use of robust physics-based models for effective battery management system design, as well as high-fidelity models based on surrogates for cloud-based digital twin applications.

CRediT authorship contribution statement

Mohammad Alipour: Conceptualization, Methodology, Software, Validation, Formal analysis, Investigation, Data curation, Writing – original draft, Writing – review & editing, Visualization. **Litao Yin:** Software. **Shiva Sander Tavallaey:** Conceptualization, Methodology, Software, Investigation, Writing – review & editing, Supervision. **Anna Mikaela Andersson:** Resources, Data curation, Project administration, Funding acquisition. **Daniel Brandell:** Conceptualization, Resources, Data curation, Writing – review & editing, Project administration, Supervision, Funding acquisition.

Declaration of competing interest

The authors declare that they have no known competing financial interests or personal relationships that could have appeared to influence the work reported in this paper.

Data availability

Data will be made available on request

Acknowledgments

Appendix A. Supplementary data

Supplementary material related to this article can be found online at https://doi.org/10.1016/j.jpowsour.2023.233273.

References

[1] Y. Wang, J. Tian, Z. Sun, L. Wang, R. Xu, M. Li, Z. Chen, A comprehensive review of battery modeling and state estimation approaches for advanced battery management systems, Renew. Sustain. Energy Rev. 131 (2020) 110015.

[2] M. Schönemann, Multiscale Simulation Approach for Battery Production Systems, Springer, 2017.

[3] N. Oreskes, K. Shrader-Frechette, K. Belitz, Verification, validation, and confirmation of numerical models in the earth sciences, Science 263 (5147) (1994) 641–646.

[4] X. Hu, L. Xu, X. Lin, M. Pecht, Battery lifetime prognostics, Joule 4 (2) (2020) 310–346.

[5] M. Alipour, S.S. Tavallaey, A.M. Andersson, D. Brandell, Improved battery cycle life prediction using a hybrid data-driven model incorporating linear support vector regression and Gaussian, ChemPhysChem 23 (7) (2022) e202100829.

[6] Y. Bar-Sinai, S. Hoyer, J. Hickey, M.P. Brenner, Learning data-driven discretizations for partial differential equations, Proc. Natl. Acad. Sci. 116 (31) (2019) 15344–15349.

[7] M.B. Mckay, B. Wetton, R.B. Gopaluni, Learning physics based models of Lithium-ion Batteries, IFAC-PapersOnLine 54 (3) (2021) 97–102.

[8] Y. Zhou, B.-C. Wang, H.-X. Li, H.-D. Yang, Z. Liu, A surrogate-assisted teaching-learning-based optimization for parameter identification of the battery model, IEEE Trans. Ind. Inform. 17 (9) (2020) 5909–5918.

[9] Z. Zheng, Y. Xu, P. Wang, Uncertainty quantification analysis on mechanical properties of the structured silicon anode via surrogate models, J. Electrochem. Soc. 168 (4) (2021) 040508.

[10] M. Doyle, T.F. Fuller, J. Newman, Modeling of galvanostatic charge and discharge of the lithium/polymer/insertion cell, J. Electrochem. Soc. 140 (6) (1993) 1526.

[11] T.F. Fuller, M. Doyle, J. Newman, Simulation and optimization of the dual lithium ion insertion cell, J. Electrochem. Soc. 141 (1) (1994) 1.

[12] M. Xu, R. Wang, P. Zhao, X. Wang, Fast charging optimization for lithium-ion batteries based on dynamic programming algorithm and electrochemical-thermal-capacity fade coupled model, J. Power Sources 438 (2019) 227015.

[13] J.M. Reniers, G. Mulder, D.A. Howey, Review and performance comparison of mechanical-chemical degradation models for lithium-ion batteries, J. Electrochem. Soc. 166 (14) (2019) A3189.

[14] J. Sturm, A. Rheinfeld, I. Zilberman, F.B. Spingler, S. Kosch, F. Frie, A. Jossen, Modeling and simulation of inhomogeneities in a 18650 nickel-rich, silicon-graphite lithium-ion cell during fast charging, J. Power Sources 412 (2019) 204–223.

[15] P. Verma, P. Maire, P. Novák, A review of the features and analyses of the solid electrolyte interphase in Li-ion batteries, Electrochim. Acta 55 (22) (2010) 6332–6341.

[16] G. Ning, B.N. Popov, Cycle life modeling of lithium-ion batteries, J. Electrochem. Soc. 151 (10) (2004) A1584.

[17] Y. Yin, Y. Hu, S.-Y. Choe, H. Cho, W.T. Joe, New fast charging method of lithium-ion batteries based on a reduced order electrochemical model considering side reaction, J. Power Sources 423 (2019) 367–379.

[18] X. Lin, J. Park, L. Liu, Y. Lee, A. Sastry, W. Lu, A comprehensive capacity fade model and analysis for Li-ion batteries, J. Electrochem. Soc. 160 (10) (2013) A1701.

[19] W.A. Appiah, J. Park, S. Byun, M.-H. Ryou, Y.M. Lee, A mathematical model for cyclic aging of spinel LiMn2o4/graphite lithium-ion cells, J. Electrochem. Soc. 163 (12) (2016) A2757.

[20] H.J. Ploehn, P. Ramadass, R.E. White, Solvent diffusion model for aging of lithium-ion battery cells, J. Electrochem. Soc. 151 (3) (2004) A456.

[21] X.-G. Yang, Y. Leng, G. Zhang, S. Ge, C.-Y. Wang, Modeling of lithium plating induced aging of lithium-ion batteries: Transition from linear to nonlinear aging, J. Power Sources 360 (2017) 28–40.

[22] P. Ramadass, B. Haran, P.M. Gomadam, R. White, B.N. Popov, Development of first principles capacity fade model for Li-ion cells, J. Electrochem. Soc. 151 (2) (2004) A196.

[23] R. Fu, S.-Y. Choe, V. Agubra, J. Fergus, Development of a physics-based degradation model for lithium ion polymer batteries considering side reactions, J. Power Sources 278 (2015) 506–521.

[24] X. Zhang, Y. Gao, B. Guo, C. Zhu, X. Zhou, L. Wang, J. Cao, A novel quantitative electrochemical aging model considering side reactions for lithium-ion batteries, Electrochim. Acta 343 (2020) 136070.

[25] Y. Zhao, S.-Y. Choe, J. Kee, Modeling of degradation effects and its integration into electrochemical reduced order model for Li (MnNiCo) O2/Graphite polymer battery for real time applications, Electrochim. Acta 270 (2018) 440–452.

[26] G. Fan, X. Li, R. Zhang, Global sensitivity analysis on temperature-dependent parameters of a reduced-order electrochemical model and robust state-of-charge estimation at different temperatures, Energy 223 (2021) 120024.

[27] W. Li, D. Cao, D. Jöst, F. Ringbeck, M. Kuipers, F. Frie, D.U. Sauer, Parameter sensitivity analysis of electrochemical model-based battery management systems for lithium-ion batteries, Appl. Energy 269 (2020) 115104.

[28] M. Lagnoni, C. Nicolella, A. Bertei, Survey and sensitivity analysis of critical parameters in lithium-ion battery thermo-electrochemical modeling, Electrochim. Acta 394 (2021) 139098.

[29] S.V. Erhard, P.J. Osswald, P. Keil, E. Höffer, M. Haug, A. Noel, J. Wilhelm, B. Rieger, K. Schmidt, S. Kosch, et al., Simulation and measurement of the current density distribution in lithium-ion batteries by a multi-tab cell approach, J. Electrochem. Soc. 164 (1) (2017) A6324.

[30] N. Paul, J. Keil, F.M. Kindermann, S. Schebesta, O. Dolotko, M.J. Mühlbauer, L. Kraft, S.V. Erhard, A. Jossen, R. Gilles, Aging in 18650-type Li-ion cells examined with neutron diffraction, electrochemical analysis and physico-chemical modeling, J. Energy Storage 17 (2018) 383–394.

[31] C. von Lüders, J. Keil, M. Webersberger, A. Jossen, Modeling of lithium plating and lithium stripping in lithium-ion batteries, J. Power Sources 414 (2019) 41–47.

[32] H. Pang, L. Mou, L. Guo, F. Zhang, Parameter identification and systematic validation of an enhanced single-particle model with aging degradation physics for Li-ion batteries, Electrochim. Acta 307 (2019) 474–487.

[33] A. Awarke, S. Pischinger, J. Ogrzewalla, Pseudo 3D modeling and analysis of the SEI growth distribution in large format Li-ion polymer pouch cells, J. Electrochem. Soc. 160 (1) (2012) A172.

[34] A. Sarkar, P. Shrotriya, I.C. Nlebedim, Parametric analysis of anodic degradation mechanisms for fast charging lithium batteries with graphite anode, Comput. Mater. Sci. 202 (2022) 110979.

[35] B. Su, X. Ke, C. Yuan, Electrochemical modeling of calendar capacity loss of nickel-manganese-cobalt (NMC)-graphite lithium ion batteries, 2021, arXiv preprint arXiv:2103.02166.

[36] M. Park, X. Zhang, M. Chung, G. Less, B, sastry AM, J. Power Sources 195 (2010) 7904–7929.

[37] M.A. Cabanero, J. Altmann, L. Gold, N. Boaretto, J. Müller, S. Hein, J. Zausch, J. Kallo, A. Latz, Investigation of the temperature dependence of lithium plating onset conditions in commercial Li-ion batteries, Energy 171 (2019) 1217–1228.

[38] X.-G. Yang, C.-Y. Wang, Understanding the trilemma of fast charging, energy density and cycle life of lithium-ion batteries, J. Power Sources 402 (2018) 489–498.

[39] M. Safari, M. Morcrette, A. Teyssot, C. Delacourt, Multimodal physics-based aging model for life prediction of Li-ion batteries, J. Electrochem. Soc. 156 (3) (2008) A145.

[40] M. Xu, Z. Zhang, X. Wang, L. Jia, L. Yang, A pseudo three-dimensional electrochemical–thermal model of a prismatic LiFePO4 battery during discharge process, Energy 80 (2015) 303–317.

[41] F. Bahiraei, M. Ghalkhani, A. Fartaj, G.-A. Nazri, A pseudo 3D electrochemical-thermal modeling and analysis of a lithium-ion battery for electric vehicle thermal management applications, Appl. Therm. Eng. 125 (2017) 904–918.

[42] L. Yin, Z. Geng, Y.-C. Chien, T. Thiringer, M.J. Lacey, A.M. Andersson, D. Brandell, Implementing intermittent current interruption into Li-ion cell modelling for improved battery diagnostics, Electrochim. Acta 427 (2022) 140888.

[43] M.D. McKay, R.J. Beckman, W.J. Conover, A comparison of three methods for selecting values of input variables in the analysis of output from a computer code, Technometrics 42 (1) (2000) 55–61.

[44] B. Sudret, S. Marelli, J. Wiart, Surrogate models for uncertainty quantification: An overview, in: 2017 11th European Conference on Antennas and Propagation (EUCAP), IEEE, 2017, pp. 793–797.

[45] T.J. Santner, B.J. Williams, W.I. Notz, B.J. Williams, The Design and Analysis of Computer Experiments, Vol. 1, Springer, 2003.

[46] T. Homma, A. Saltelli, Importance measures in global sensitivity analysis of nonlinear models, Reliab. Eng. Syst. Saf. 52 (1) (1996) 1–17.